JOURNAL OF MATERIALS SCIENCE 28 (1993) 4471–4482

Stress analysis of elastomeric materials at large extensions using the finite element method

Part II *Stress and strain distribution around rigid spherical particles*

Y. FUKAHORI, W. SEKI
Research and Development Division, Bridgestone Corporation, Kodaira-shi, Tokyo 187, Japan

The finite element method is applied to stress and strain analyses around rigid spherical particles in elastomers at large extensions. The stress and strain distribution computed agree well with the classical theoretical ones at small strain. At large extension, however, the maximum stress concentration factor increases greatly and the maximum strain concentration factor decreases slightly as strain increases. These tendencies are increased more in carbon black-filled elastomers than in unfilled ones, which can be understood reasonably by considering both the geometric and material non-linearity. Reinforcement of elastomers with rigid spherical particles was also analysed through a numerical computation. The computed results agree with the Guth and Mooney equations at low volume fraction of fillers. In carbon black-filled elastomers, on the other hand, where the modulus is much higher than that given by the above equations, the computations give a good agreement with the experiments, considering the 20% increase in effective diameter of the filler.

1. Introduction

The addition of rigid spherical particles to polymeric materials is significantly important from the viewpoints of fracture initiation and filler reinforcement. Particularly in elastomers, most rubber articles of practical use are reinforced with carbon blacks, which gives rise to greatly improved mechanical properties of rubber compounds. A large number of studies has been reported for reinforcement of elastomers with carbon blacks, whose models are fundamentally based on Einstein's equation for the increase of viscosity by the addition of fillers. On the other hand, it is well known that there is a critical value of applied stress at which a cavity nucleates around a rigid spherical inclusion embedded in an elastomeric material subjected to an axisymmetrical load. As Oberth and Bruenner observed [1], a small cavity appeared within the matrix near a pole of the inclusion in the case of strong bonding at the particle–matrix interface when the applied uniaxial stress reached a certain critical value. This is considered to be consistent with the results obtained from the stress analysis given by the classical solution.

It is quite surprising, however, that actual stress analyses have been rarely performed around a rigid sphere embedded in elastomeric materials, except for just a few empirical results, despite the fact that a tremendous amount of research on fracture phenomena and reinforcement in particle–elastomer systems has been reported. One of the most serious reasons why stress analysis in these systems has not been widely carried out is the difficulties in the numerical techniques such as a finite element analysis. As is well known, because a finite element method is based originally on the classical or small strain linear elasticity theory, there exist several difficulties which have to be overcome for the application of FEM to elastomers, concerning non-linear stress–strain relations and the incompressible behaviour of the elastomer, in addition to its tremendous amount of deformation over several hundred per cent in failure.

In Part I [2], we applied a newly developed finite element analysis to stress and strain analyses around a spherical hole in elastomers from small to very large extensions near their break and obtained the following conclusions.

1. Stress and strain distributions around a spherical hole subjected to uniaxial tensile strain are similar to those given by classical theoretical solutions at small strain but they deviate from the classical theoretical ones as the strain increases.
2. The maximum stress concentration factor increases and the maximum strain concentration factor decreases with increasing average strain. These tendencies are increased more in carbon black-filled elastomers than in unfilled ones.
3. A successful description of these phenomena can be achieved by considering the non-linear properties in the stress–strain relation of rubber vulcanizates which increase as extension increases and carbon black content increases.

0022–2461

In Part II we apply a new numerical method to stress and strain analyses around a rigid spherical particle in an elastomeric material at large extension, and establish quantitative and systematic analyses for the fundamental bases of fracture and reinforcement in elastomers.

2. Theoretical background

2.1. Stress concentration around a rigid spherical inclusion

According to classical elasticity theory [3], the stress around a spherical inclusion, whether it is a hole or rigid particle, represented in terms of the polar coordinate system (Fig. 1), is given by Equations 1–7 in Part I [2], provided that constants A, B and C in these equations for a rigid particle are given by

$$A = \frac{r_0^3\sigma_0}{4E}\frac{13-10\nu}{7-5\nu},$$

$$B = -\frac{r_0^5\sigma_0}{8E}\frac{1}{7-5\nu},$$

$$C = -\frac{r_0^3\sigma_0}{8E}\frac{5(1-2\nu)}{8-10\nu}.$$

Oberth [4] and Oberth and Bruenner [1] studied the stress distribution around a steel sphere embedded in polyurethane rubber using a photoelastic method and made clear that the maximum stress is a small distance away from the particle surface as was predicted by classical elasticity theories. Moreover, Oberth and Bruenner [1], Gent and Park [5] and Cho and Gent [6] showed that a small cavity appeared abruptly within the matrix near the poles of the particle when the applied uniaxial stress reached a certain critical value. It is incredible, however, that stress analysis around a rigid spherical inclusion in elastomers is missing except for the classical solution and a few experimental analyses [1, 4]. Although a few papers [6, 7], have tried a brief finite element analysis for a rigid inclusion in elastomers, they are based on the assumption of the linear stress–strain relation in materials and are not valid for general stress analysis of real non-linear elastomeric materials under such large deformations in which a cavitation or crack occurs. As will be shown later, the accuracy of computation strictly depends on how accurate information can be introduced concerning the characteristics of materials, i.e. the strain-energy function of the material applicable for a wide range and wide mode of deformation.

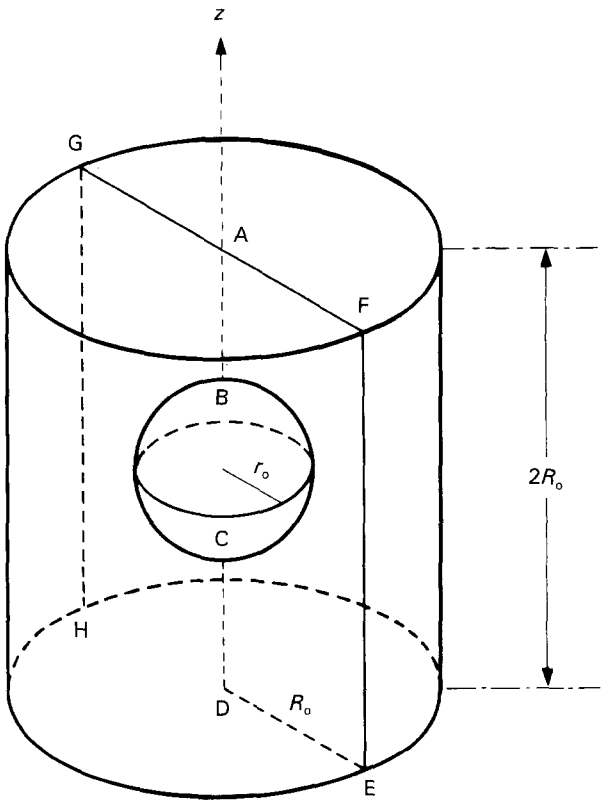

Figure 1 A cylinder of matrix containing a single sphere at its centre.

2.2. Theories of rigid filler reinforcement for elastomers

Many theories have been proposed to describe filler reinforcement for elastomers. The earliest idea for filler reinforcement is based on Einstein's equation [8], in which the increase of the viscosity of a liquid by the addition of uniform spherical inclusions is calculated by

$$\eta = \eta_0(1 + 2.5v) \quad (1)$$

where η and η_0 are the viscosity of the composite and the matrix liquid, respectively, and v is the volume fraction of the fillers. Guth [9] generalized the Einstein concept by introducing the interaction between the spheres as Equation 2

$$G = G_0(1 + 2.5v + 14.1v^2) \quad (2)$$

where G and G_0 are the shear moduli of the composite and the matrix, respectively. Moreover, Mooney [10] proposed a slightly different equation considering the crowding factor, s (=volume occupied by the filler/true volume of the filler), $s = 1.35$ for close packed spheres

$$G = G_0 \exp\left(\frac{2.5v}{1-sv}\right) \quad (3)$$

Although most of these theories assume perfect adhesion between the filler and the polymer matrix, Sato and Furukawa [11] discussed the case of imperfect adhesion between them, where they treated the non-bonded particles as special holes which produce a small increase in modulus.

Some of these equations have been proved to be valid in a number of fillers except carbon blacks. The strong reinforcing effect of carbon blacks for elastomers is argued by many researchers [12–17] who considered the rubber absorbed on the surface of carbon blacks, called bound rubber or occluded rubber. The absorbed rubber is insoluble in originally good rubber solvents and forms an insoluble gel with the filler. The absorbed rubber appears in a glassy state and is regarded as part of the carbon black, whose thickness is assumed to be of the order of a few

nanometres. Therefore, the high reinforcing effect of carbon blacks on elastomers may be due to the volume fraction of filled carbon blacks.

3. Experiments and numerical treatments

3.1. Materials and their strain-energy function

The materials used here are unfilled (NR1), slightly filled (NR2) and heavily filled (NR3) natural rubber vulcanizates with carbon blacks. The relevant compounding recipes are given in Part I [2]. NR2 was mostly used for computation, unless noted otherwise. Strain energy function, W, is determined through strip-biaxial (pure shear) testing with a newly designed apparatus. As indicated in detail elsewhere [18–21], $\partial W/\partial I_1$ and $\partial W/\partial I_2$ are not constants but have typical features varying with I_1 and I_2, which indicates that the stress–strain relation of real elastomers cannot be represented by a simple linear relation, particularly under large deformation. The accuracy of the numerical method strongly depends on how accurate is the W function used for the calculation, and it seems to be the best way at the present technical level to evaluate empirically the W function through biaxial testing.

3.2. The numerical model

As the theoretical backgrounds of the finite element method (FEM) have already been described in detail in Part I [2], we will only give a brief outline of the newly developed FEM in this report. The method includes two important points. First, the strain-energy function of real elastomers, the elastic energy stored in a deformed body, is experimentally evaluated through strip-biaxial (pure shear) testing. Second, computer programming has been improved based on the mixed variational method to treat the problems of incompressibility in elastomers.

Spherical inclusions randomly distributed in a finite matrix can be represented by a cylinder of matrix containing a single sphere of a radius r_0 at its centre, its radius and the height being R_0 and $2R_0$, respectively, in a finite element analysis, as shown in Fig. 1. Two assumptions are introduced: infinitely high modulus of a solid sphere and a perfect bonding between solid spheres and matrix elastomers. The cylinder can be predicted by the plane ABCDEF using axisymmetric elements, the z-axis being the axis of symmetry. The boundary conditions which must be satisfied in the calculation are as follows (shown in Fig. 1).

1. The surface of the solid sphere is perfectly constrained, that is, the sphere cannot be deformed at its interface (Fig. 2).
2. No constraint is imposed on the side surface of the cylinder, i.e. free deformation and no external force.
3. The circular surface of the cylinder is constrained to remain perpendicular to the z-axis, but freely deformable in the x-direction.

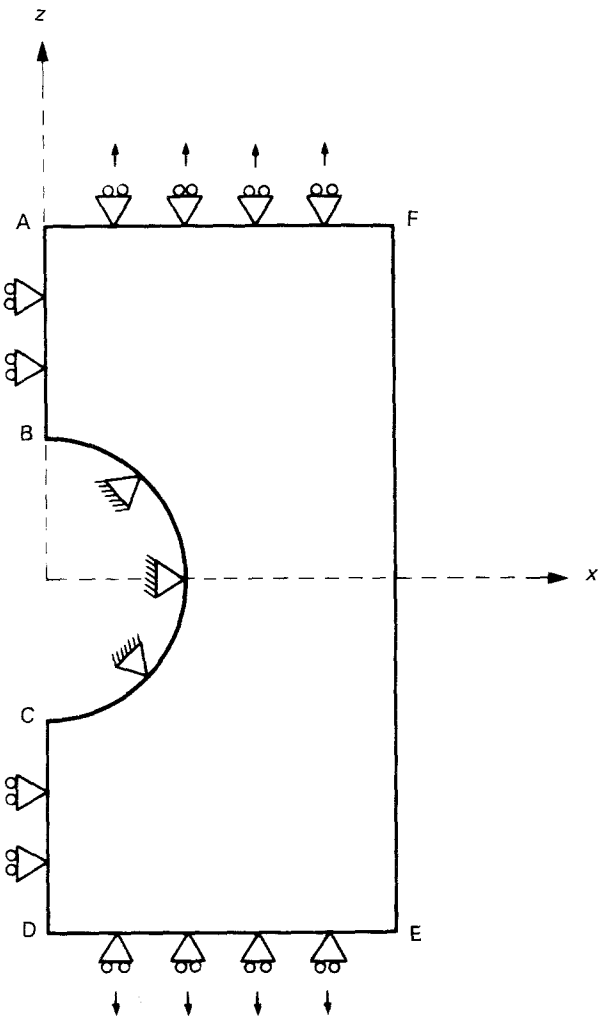

Figure 2 The plane ABCDEF given in Fig. 1 using axisymmetric elements, the z-axis being the axis of symmetry.

The deformation of the grid is achieved by loading the grid (a uniform stress, σ_0) by prescribed displacement in the z-direction.

The volume fraction v of spheres which occupy the system can be calculated by the relation, $v = 2/3(r_0/R_0)^3$. An increase in the value of the geometrical parameter r_0/R_0 is equivalent to the spheres being close together. In the present computation, the radius of the sphere, r_0, was kept constant, while that of the cylinder was varied, the relation between the geometric parameter, r_0/R_0, and volume fraction, v, being given in Table I.

The computation gives the maximum principal stress (true stress), σ, and the maximum principal strain, ε. Uniform (average) stress applied to the system, σ_0, is calculated from the sum of the force applied to a circular surface of the cylinder divided by its surface area. All stress and strain fields are represented by the stress concentration factor α $(=\sigma/\sigma_0)$ and strain concentration factor β $(=\varepsilon/\varepsilon_0)$ and the maximum stress and strain concentration factors, α_{max} and β_{max}, respectively.

Moreover, in this paper, we performed a three-dimensional simulation for a square pillar of matrix elastomers containing a single sphere at its centre. Although two-dimensional simulation for a cylinder is

TABLE I Relation between the geometric parameter, r_0/R_0, and volume fraction, v

r_0/R_0	v (%)
1/12	3.85×10^{-2}
1/5	5.33×10^{-1}
1/2	8.33
1/1.5	1.98×10
1/1.2	3.85×10

quite useful for stress analysis around an inclusion or at a corner and edge with sufficiently high accuracy, because it is easy to give very fine meshes in two-dimensional simulation, cylinders cannot fill up the space. On the other hand, although it is difficult to give fine meshes in three-dimensional simulation, cubes can fully fill up the space and thus give better natural boundary conditions for estimating the total figures in dynamics, such as the stress–strain relation and filler reinforcement. In this paper, we used three-dimensional simulation only for the analysis of filler reinforcements, as shown in Fig. 3. The boundary conditions are almost the same in both the two- and three-dimensional simulations, except that all deflections perpendicular to the z-axis on the side surface of the cube are constrained to be equal in the three-dimensional simulation. Fig. 4 gives the finite element model for the three-dimensional computation.

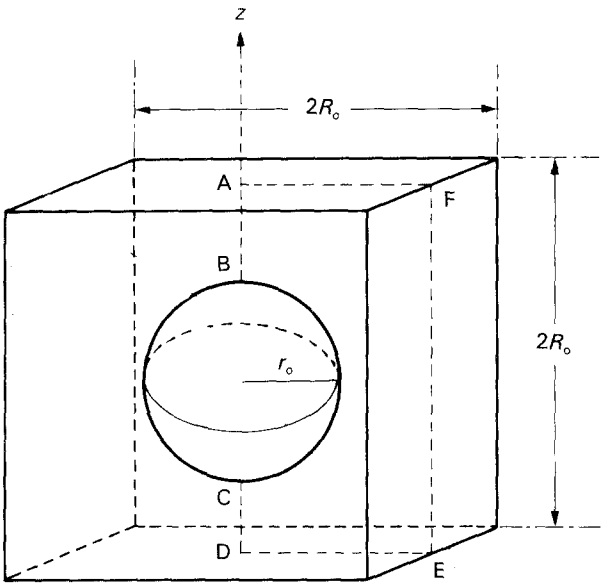

Figure 3 A cube of matrix containing a single sphere at its centre.

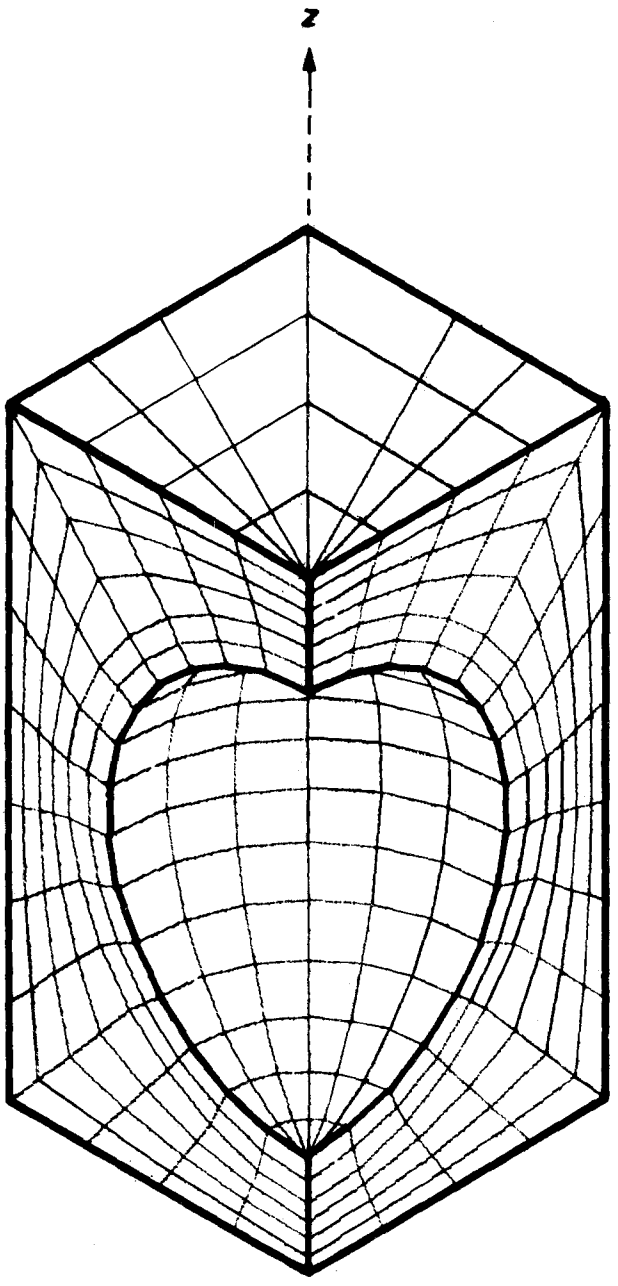

Figure 4 Finite element model for the three-dimensional computation.

4. Results and discussion

4.1. Stress and strain distribution around rigid spherical particles subjected to uniaxial tensile stress

4.1.1. Theoretical solutions

The stresses predicted in the polar coordinates are given by six polar elements (σ_{rr}, $\sigma_{\varphi\varphi}$, $\sigma_{\theta\theta}$, $\sigma_{r\varphi}$, $\sigma_{r\theta}$, $\sigma_{\theta\varphi}$) as shown in Equations 1–5 in Part I [2]. In this paper we used three principal stresses, σ_i ($i = 1, 2, 3$) and the maximum principal stress between them by solving Equation 4

$$\begin{vmatrix} \sigma_{rr} - \sigma & \sigma_{r\varphi} & \sigma_{r\theta} \\ \sigma_{r\varphi} & \sigma_{\varphi\varphi} - \sigma & \sigma_{\theta\varphi} \\ \sigma_{r\theta} & \sigma_{\theta\varphi} & \sigma_{\theta\theta} - \sigma \end{vmatrix} = 0 \quad (4)$$

Although, in other works [1, 4], the polar element is directly used for stress analysis, we use the maximum principal stress, σ, and the maximum principal strain, ε, because these parameters seem to play more important roles in studies of fracture analysis and filler reinforcement.

Figs 5 and 6 are theoretical contour maps of stress concentration factor, σ_{rr}/σ_0, and strain concentration factor, $\varepsilon_{rr}/\varepsilon_0$, around a rigid spherical particle subjected to uniaxial stress represented on the undeformed coordinates. As reported by Oberth and Bruenner [1], the maximum stress and the maximum strain appears at a point slightly away from the poles along the z-axis, and their absolute values are 2.30 and 1.71, respectively. However, contour maps of stress and strain concentration factors exhibited by

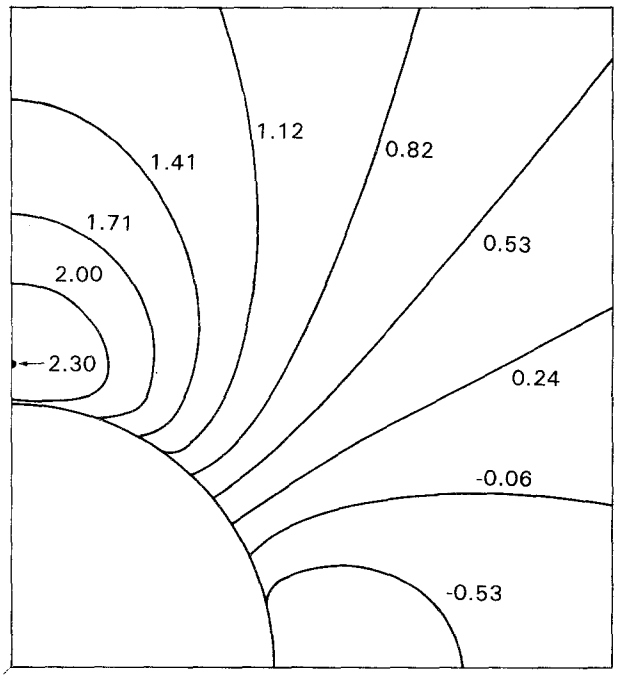

Figure 5 Theoretical contour maps of stress concentration factor, σ_{rr}/σ_0 around a rigid spherical particle represented on the undeformed coordinates.

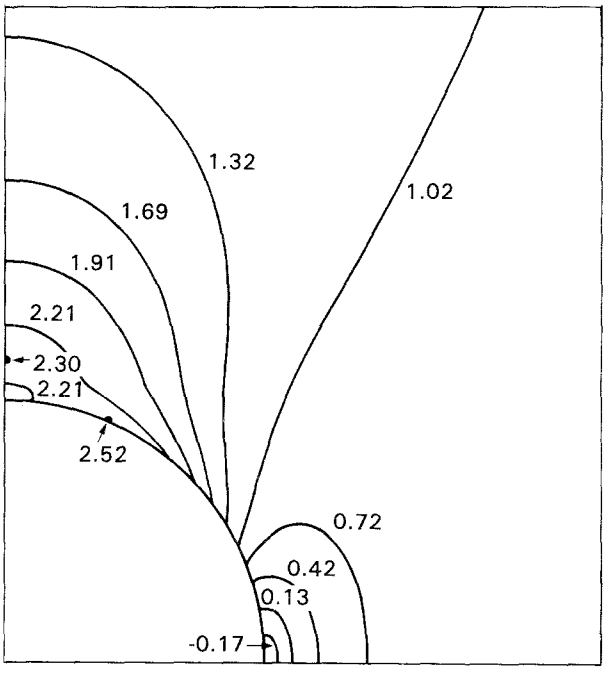

Figure 7 As Fig. 5, but of stress concentration factor exhibited by the maximum principal stress, σ/σ_0 ($=\alpha$).

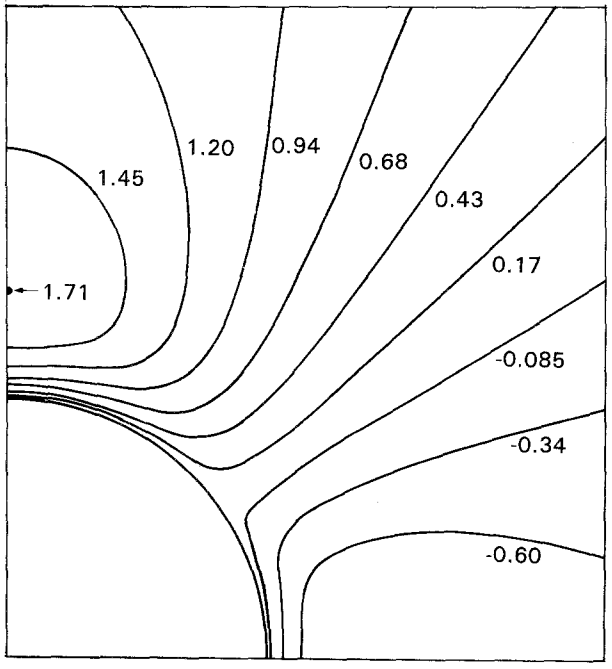

Figure 6 As Fig. 5, but of strain concentration factor, $\varepsilon_{rr}/\varepsilon_0$.

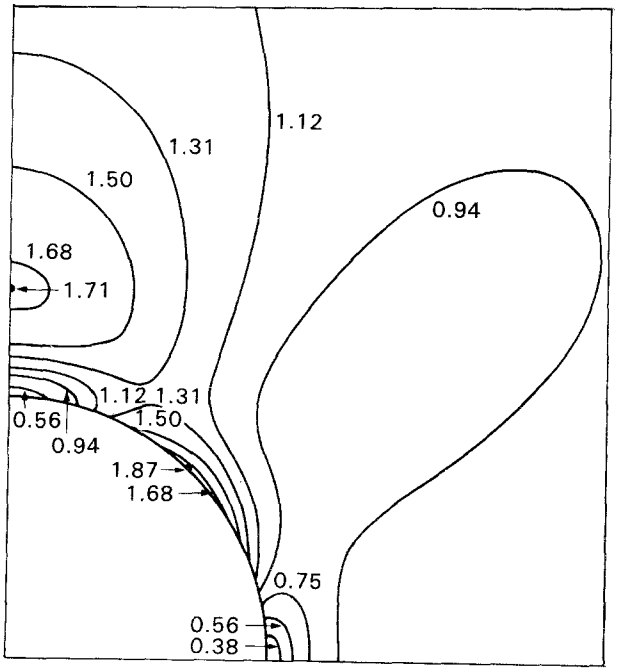

Figure 8 As Fig. 6, but of strain concentration factor exhibited by the maximum principal strain, $\varepsilon/\varepsilon_0$ ($=\beta$).

the maximum principal stress and the maximum principal strain give slightly different features. In Fig. 7, although there is a high stress concentration of the same value seen near the pole of the particle, the maximum stress concentration occurs on the surface of the particle at $\theta = 23°$, the value being 2.52. Fig. 8 also gives the maximum strain concentration at $\theta = 43°$, the value being 1.87 in addition to a high strain concentration along the z-axis, 1.71. Cavities which appeared not only on the pole but near other parts of the surface [1, 3–5] within the matrix elastomers seem to prove that the expression by the maximum principal stress and strain is more preferable than that by the direct polar elements.

4.1.2. Numerical results computed at $r_0/R_0 = 1/12$

Now we show contour maps of α and β around a rigid spherical particle computed under the condition of $r_0/R_0 = 1/12$, in which the disturbance by adjacent particles in stress and strain distribution can be neglected.

Figs 9 and 10 correspond to the case of a small average strain ($\varepsilon_0 = 10\%$). It is clearly seen that the stress and strain distribution around a rigid spherical particle and their absolute values computed by the numerical method based on the strain-energy function obtained experimentally agree well with theoretically calculated ones given in Figs 7 and 8, when the average strain is small. On the other hand, contour maps give different features at large average strain. Fig. 11 is a contour map of stress concentration factor computed at $\varepsilon_0 = 100\%$. Both stress concentration factors appearing at $\theta = 30°$ and at a point along the z-axis are considerably larger than theoretical ones, and the maximum stress concentration changes its position from $\theta = 30°$ to $\theta = 0$, i.e. along the z-axis as shown in Fig. 11. When an average strain is 200% (Fig. 12), the maximum stress concentration occurs along the z-axis and its absolute value ($\alpha_{max} = 4.93$) becomes much higher than the theoretical one ($\alpha_{max} = 2.30$). On the other hand, the strain distribution and the maximum strain concentration factor around a hard spherical particle are almost independent of average strain, which is shown in Figs 13 ($\varepsilon_0 = 100\%$) and 14 ($\varepsilon_0 = 200\%$).

These situations are understood more clearly by the plots of α and β against the distance from the surface of the filler along the z-axis and the x-axis. Fig. 15 is

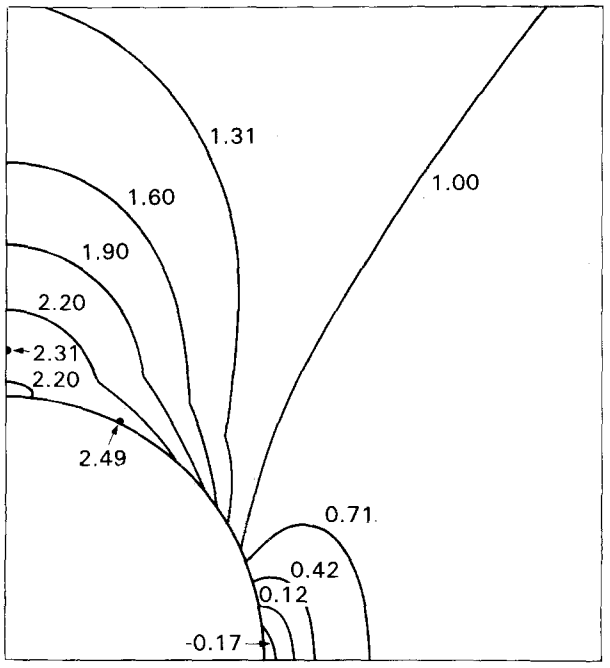

Figure 9 Contour maps of α around a rigid spherical particle computed at $\varepsilon_0 = 10\%$ and $r_0/R_0 = 1/12$.

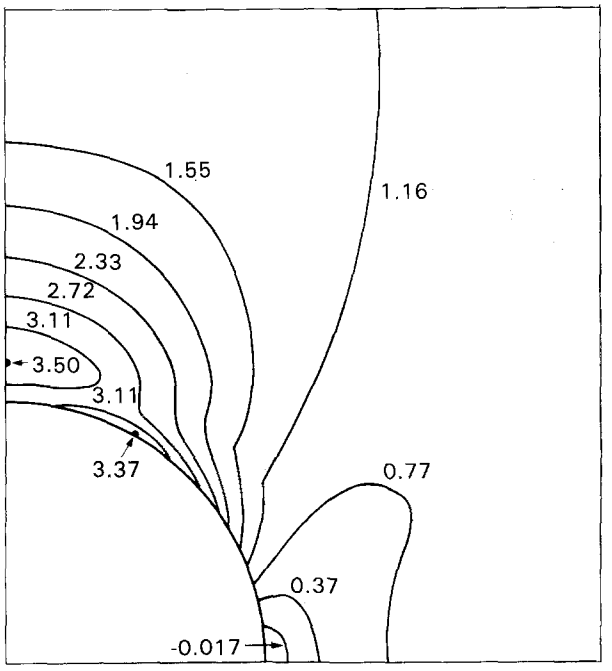

Figure 11 As Fig. 9, but at $\varepsilon_0 = 100\%$ and $r_0/R_0 = 1/12$.

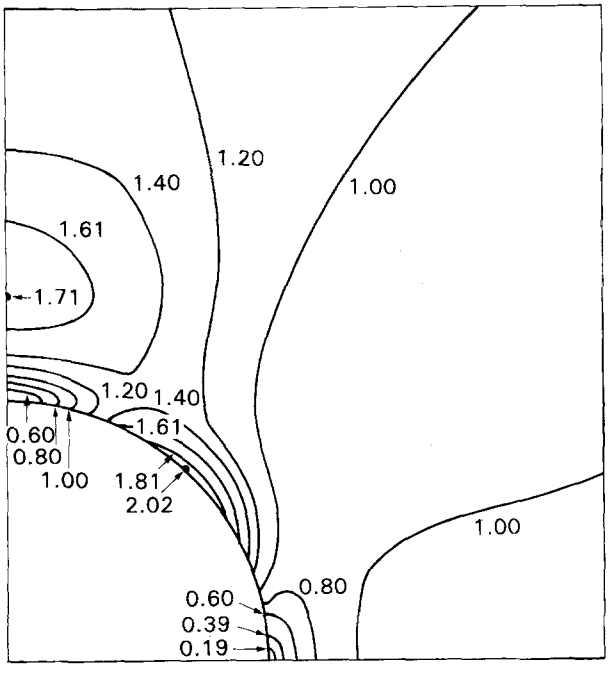

Figure 10 As Fig. 9, but of β.

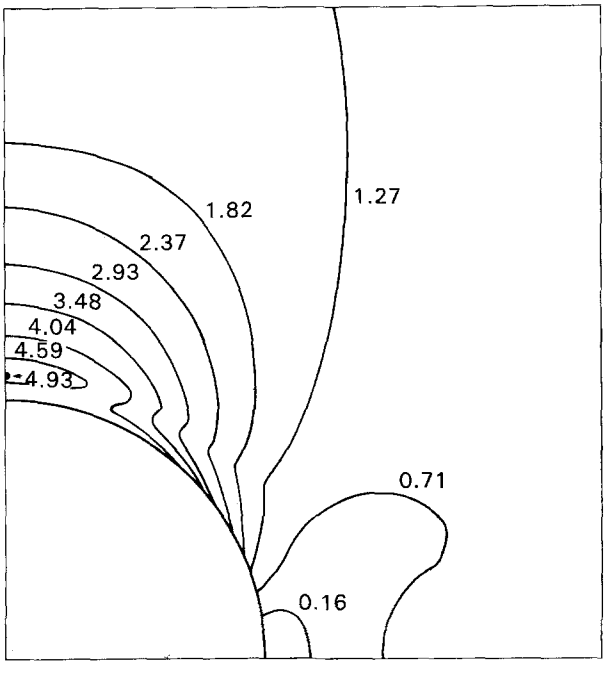

Figure 12 As Fig. 9, but at $\varepsilon_0 = 200\%$ and $r_0/R_0 = 1/12$.

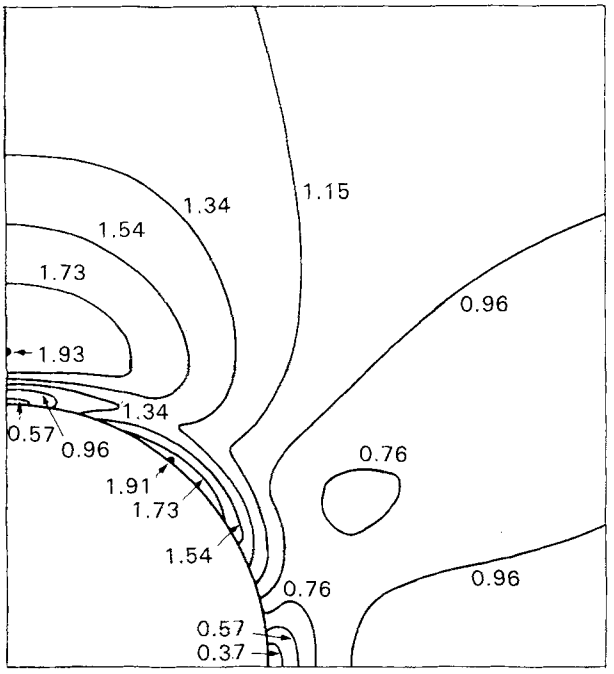

Figure 13 As Fig. 10, but at $\varepsilon_0 = 100\%$ and $r_0/R_0 = 1/12$.

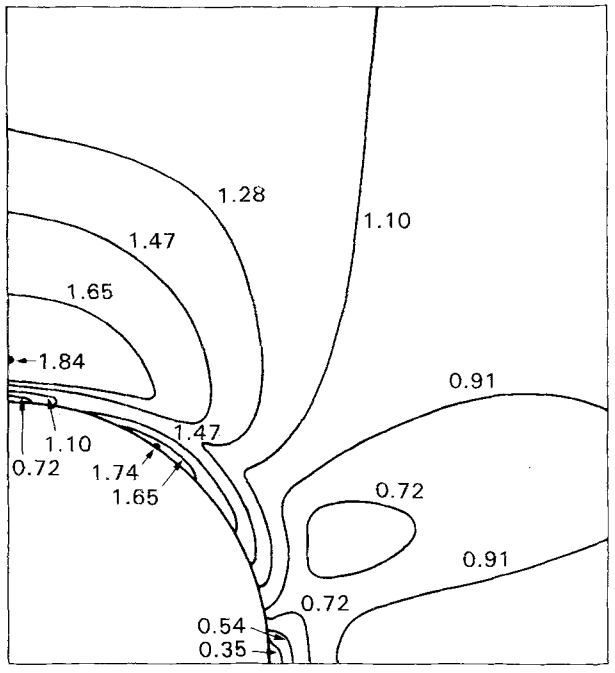

Figure 14 As Fig. 10, but at $\varepsilon_0 = 200\%$ and $r_0/R_0 = 1/12$.

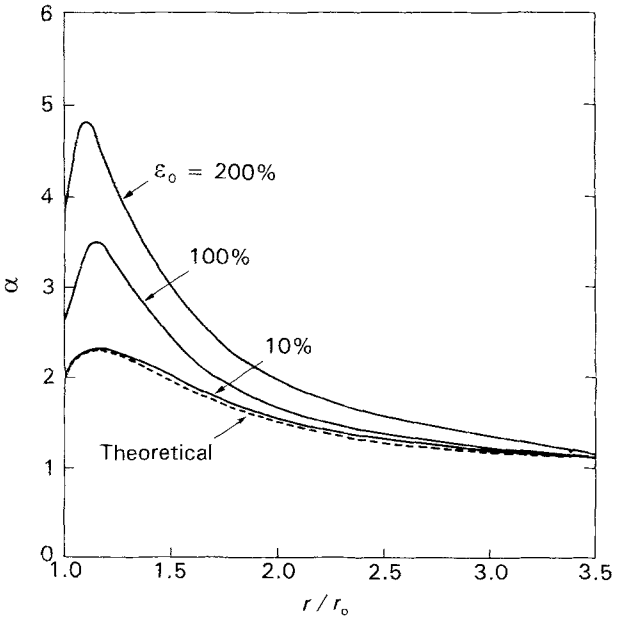

Figure 15 α as a function of r/r_0 along the z-axis at various strains.

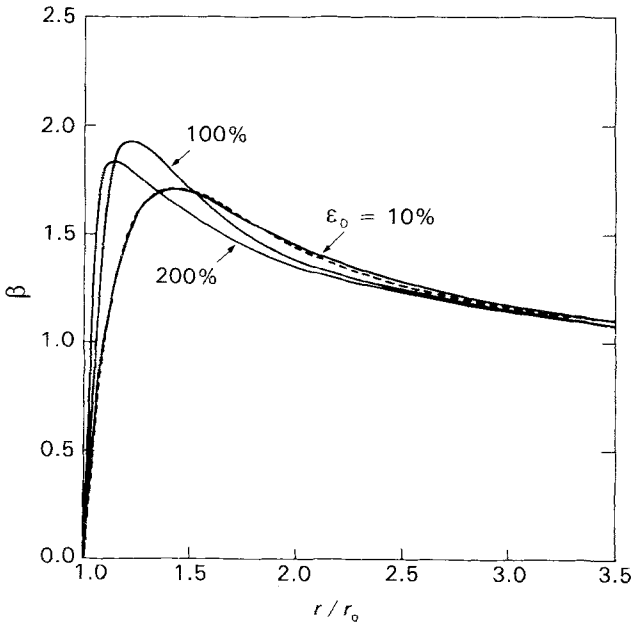

Figure 16 β as a function of r/r_0 along the z-axis at various strains. (- - -) Theoretical.

the distribution of α plotted as a function of the position, r/r_0, at various average strains along the z-axis. When the average strain is less than 10%, the α–r/r_0 curve makes a good fit with the theoretical one. As the average strain increases, however, the α–r/r_0 curves rapidly increase, particularly at the small distance r, which finally produces a very high value of α_{max}, despite the fact that the position which gives α_{max} seems to be independent of the magnitude of average strain. On the other hand, the β–r/r_0 curves plotted as a function of the position along the z-axis are little influenced by the magnitude of average strain, as shown in Fig. 16.

It is shown that the plots of α and β against the distance along the x-axis are almost independent of the magnitude of average strain, as shown in Figs 17 and 18, respectively.

4.1.3. Numerical results computed at $r_0/R_0 = 2/3$

Stress and strain distribution around a rigid spherical particle are strongly disturbed by adjacent particles. Fig. 19 is a contour map of α computed at $r_0/R_0 = 2/3$ corresponding to the case of strong interaction with adjacent particles, where it is seen that the high stress region spreads over the adjacent particles along the z-axis. In Fig. 20 the maximum strain concentration

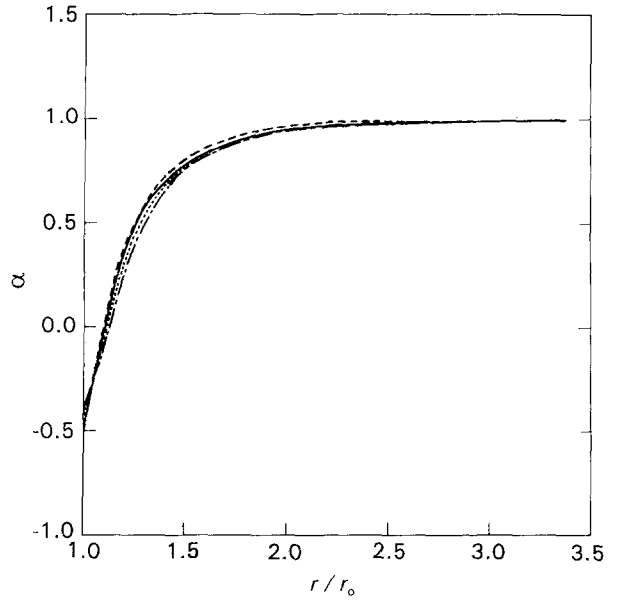

Figure 17 As Fig. 15, but along the x-axis. (– – –) Theoretical; ε_0: (—) 10%, (- - -) 100%, (— - —) 200%.

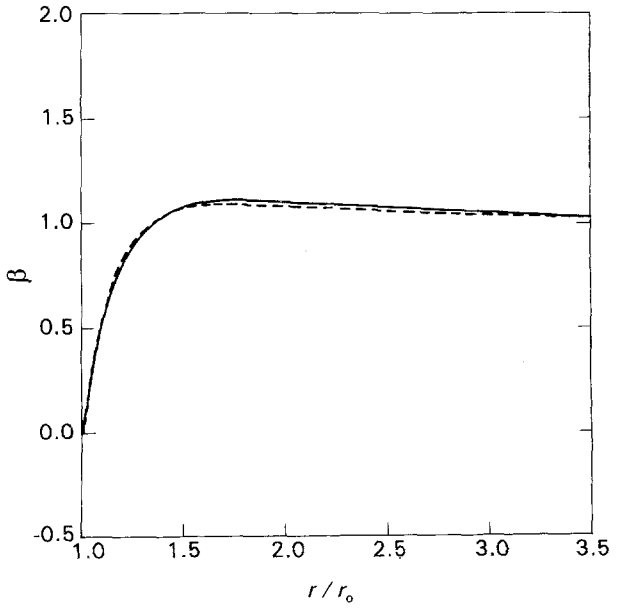

Figure 18 As Fig. 16, but along the x-axis. (- - -) Theoretical; (——) $\varepsilon_0 = 200\%$.

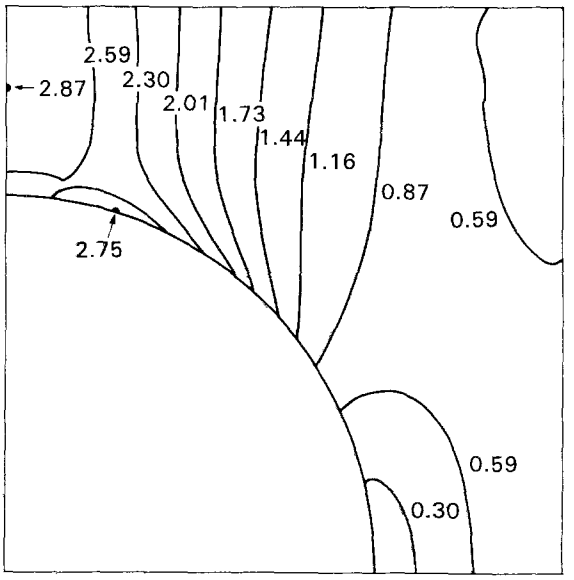

Figure 19 Contour maps of α computed at $\varepsilon_0 = 10\%$ and $r_0/R_0 = 2/3$.

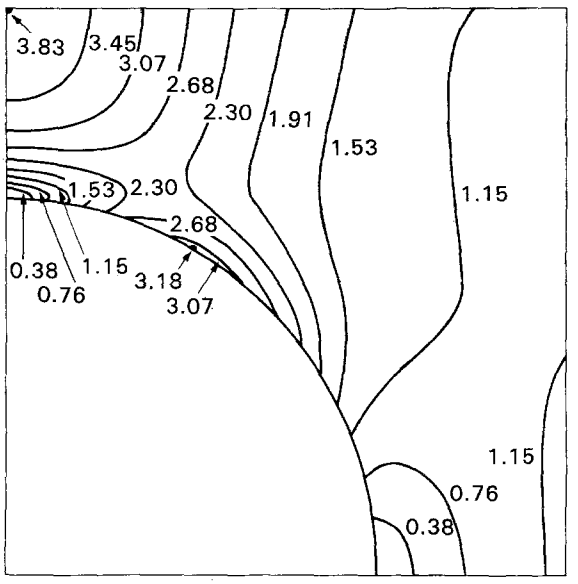

Figure 20 As Fig. 19, but of β.

factor, β_{max}, is at the boundary of the cylinder, i.e. the centre between two adjacent particles along the z-axis. Figs 21 and 22 give clearer images of the strong increase in α_{max} and β_{max} as a function of r_0/R_0 respectively.

4.1.4. Relation between increase of stress concentration and non-linearity in elastomers at large deformation

As we have seen so far, much higher stress concentration and slightly lower strain concentration occur around a rigid spherical particle when the particle is subjected to a large average strain, compared with the classical theoretical values. In Part I [2] we discussed the reason why α_{max} and β_{max} around a spherical hole change their magnitudes deviating from the classical theoretical values as the average strain increases, in relation to geometric and material non-linearity under large extension. In the case of a spherical hole, although both geometric and material non-linearity play important roles in the deviation of α_{max} and β_{max} from the classical (infinitesimal strain) theoretical solution, we concluded that the main contribution to the increase of α_{max} and the decrease of β_{max} resulted from the material non-linearity in elastomers, which increases as extension increases and also as filler content increases.

Figs 23 and 24 are α_{max} and β_{max} computed and plotted as a function of strain amplitude in three rubber vulcanizates, NR1 (unfilled), NR2 (slightly filled) and NR3 (heavily filled). Although, in all materials, α_{max} greatly increases as average strain increases, β_{max} shows a slight decrease with increasing

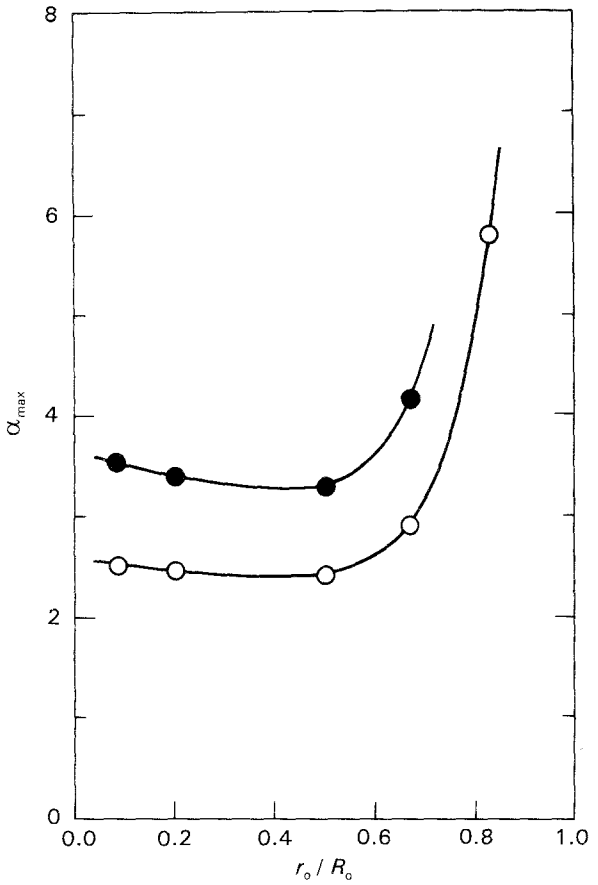

Figure 21 α_{max} as a function of r_0/R_0. ε_0: (●) 100%, (○) 10%.

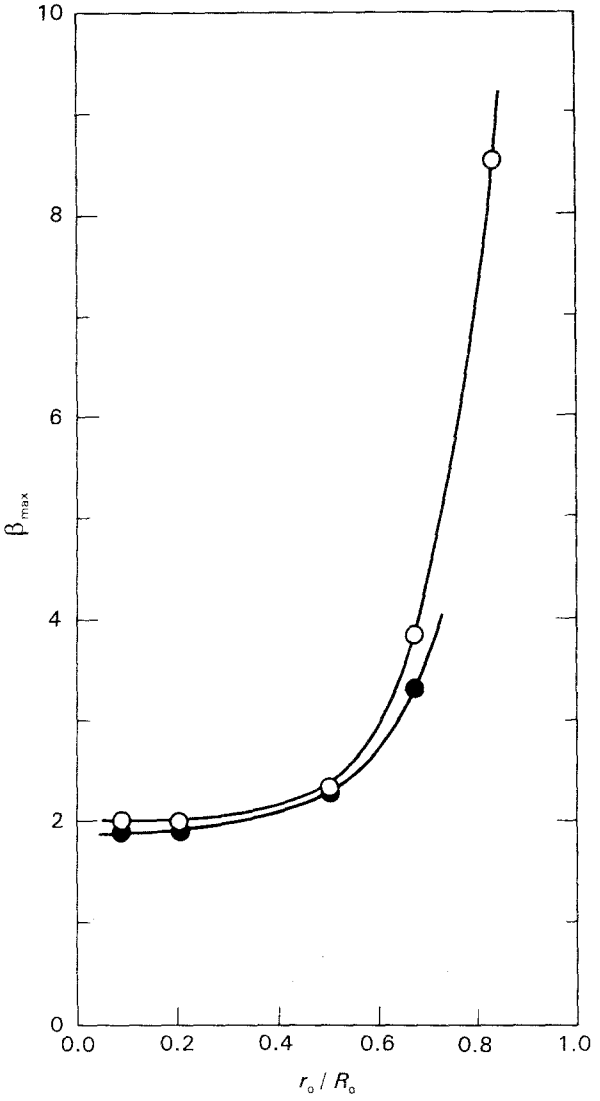

Figure 22 β_{max} as a function of r_0/R_0. ε_0: (●) 100%, (○) 10%.

average strain, whose tendency is seen most apparently in heavily reinforced rubber, NR3. As explained in detail in Part I [2], Yang [22] calculated α_{max} and β_{max} under moderately large extension for a rigid circular inclusion, using the strain-energy function of the Mooney material. The results thus calculated for a rigid inclusion in the Mooney material are the same as for a spherical hole, that is, α_{max} increases greatly and β_{max} increases slightly as the average strain increases, due to geometric non-linearity. Fig. 23 in our numerical results suggests that in the discrepancy between α_{max} thus computed and the classical theoretical solution, geometric non-linearity makes a greater contribution than material non-linearity.

However, Fig. 24 shows that the decrease of β_{max} with increasing strain amplitude in elastomers cannot be interpreted by geometric non-linearity, and should be attributable to the material non-linearity. Therefore, what we can say at the present stage of the research is that both geometric and material non-linearity play important roles in the deviation of α_{max} and β_{max} from the classical theoretical solution as extension increases.

The facts that α_{max} increases and β_{max} decreases with increasing strain amplitude in elastomeric materials can be interpreted by considering the material non-linearity of elastomers, i.e. the stress hardening under large extension, as seen in Part I [2]. That is, we can see that under large extension, the elastomer component which surrounds a spherical rigid particle gradually increases the stiffness as it approaches the boundary

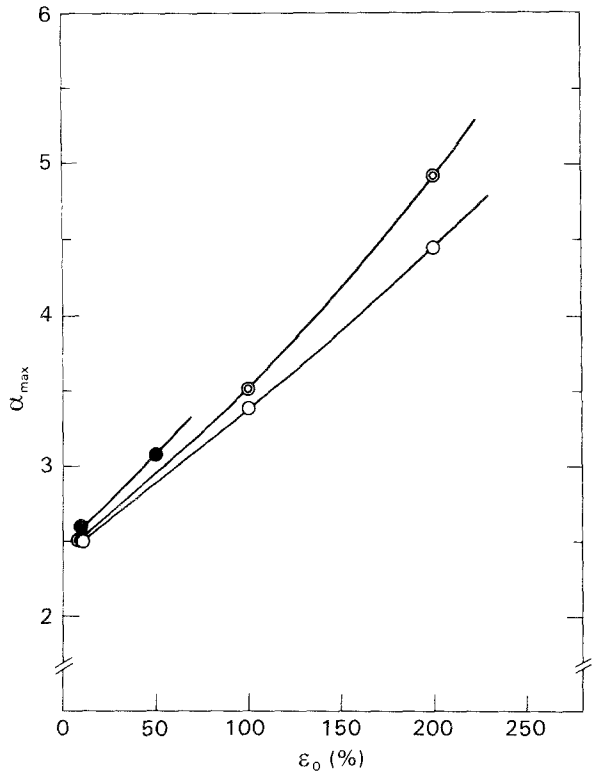

Figure 23 α_{max} plotted against strain for three rubber vulcanizates: (○) NR1, (◎) NR2, (●) NR3.

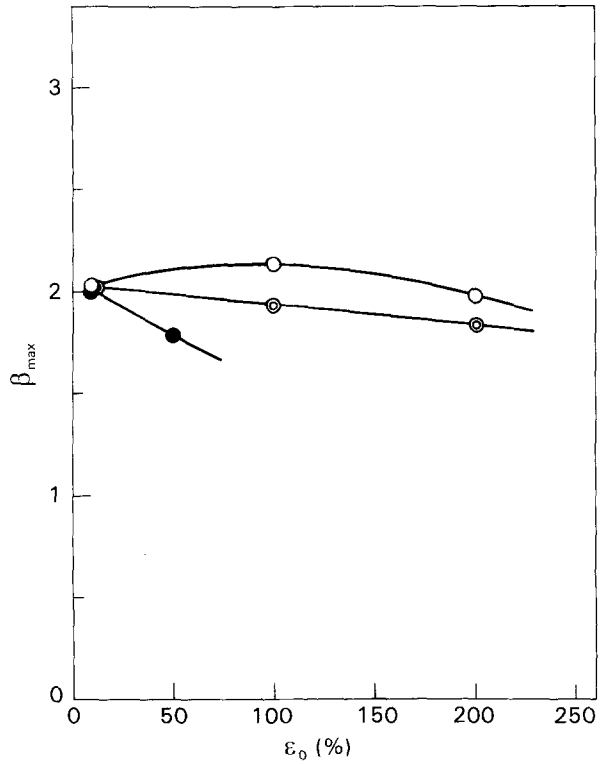

Figure 24 β_{max} plotted against strain for three rubber vulcanizates: (○) NR1, (◎) NR2, (●) NR3.

of the particle. In other words, the system which surrounds the particle can be regarded as being constructed of components of different stiffness when it is highly strained. A detailed explanation is given in Part I [2].

4.2. Filler reinforcement for elastomers

Now let us consider reinforcement of elastomers with carbon blacks through a numerical method. As explained earlier, for the purpose of elucidating the mechanism of filler reinforcement, we performed three-dimensional simulation with a cube of matrix elastomers containing a single sphere at its centre. Figs 25 and 26 are examples of such a simulation, i.e. the contour maps of α and β at an average strain of 10% and $r_0/R_0 = 2/3$ corresponding to Figs 19 and 20 performed in two-dimensional computation, respectively. A slight disagreement between both computations arises from the rough meshing in three-dimensional computation. In Fig. 27 the ratio of the modulus of the composite filled with rigid spherical particles, G, to that of the unfilled matrix rubber, G_0, is plotted against the volume fraction of filler, v. The solid curve, computed (1), in Fig. 27, is the computed result based on the strain-energy function of the unfilled rubber vulcanizate, which is compared with other theoretical dotted curves given by Equations 1–3. The computed result seems to agree with the Guth and Mooney equations at $v \leq 0.25$. On the other hand, open circles in Fig. 27 are empirically obtained at 10% strain in a simple extension test for rubber vulcanizates filled with carbon blacks of various volume fractions. Obviously the experimental results are much higher than the computed and calculated ones.

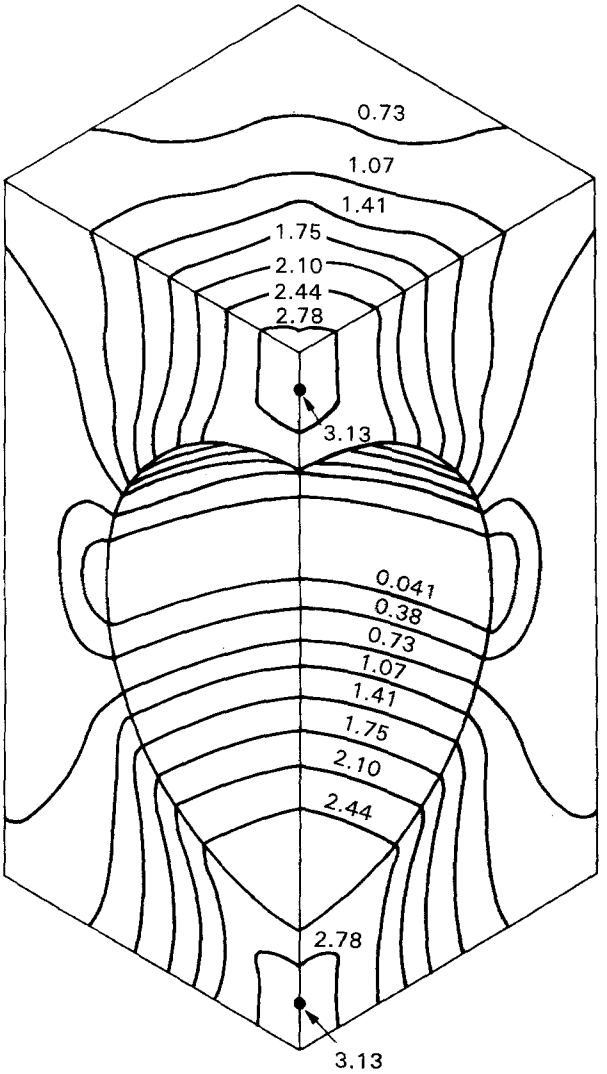

Figure 25 Contour maps of α at $\varepsilon_0 = 10\%$ and $r_0/R_0 = 2/3$ computed in a three-dimensional condition.

As has been discussed in the literature [12–17], the strong reinforcement by carbon blacks is considered to be attributable to the increase of filler surface, i.e. the increase of the diameter of filler, composed of the glassy state of rubber molecules (gel). The thickness of the increased diameter has been decided to be of the order of a few nanometres through many kinds of analytical method, such as solvent adsorption, electron microscope and the pulsed NMR. Therefore, we attempted to calculate the modulus of reinforced rubbers assuming that a carbon black is surrounded by a surface layer of glassy-state rubber whose modulus is 1000 times higher than that of the matrix rubber, that is, the strain-energy function of the surface layer is assumed to be 1000 times higher than that of the unfilled rubber and its thickness is 10% of the diameter of the particle, as shown in Fig. 28. Filled circles, computed (2), in Fig. 27 are results thus computed for various filler contents. Considerably good agreement between computations and experiments is realized. Because the diameter of a carbon black used in the present paper, HAF carbon black, is roughly 20–30 nm, the thickness of the surface layer will be 2–3 nm, whose thickness agrees well with that given in the literature.

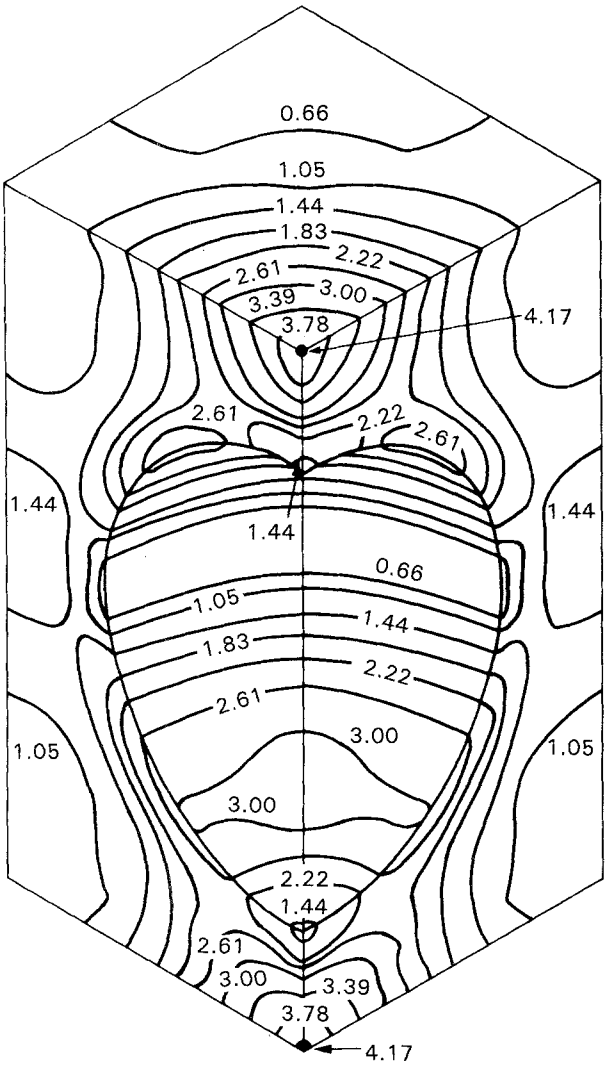

Figure 26 As Fig. 25, but of β.

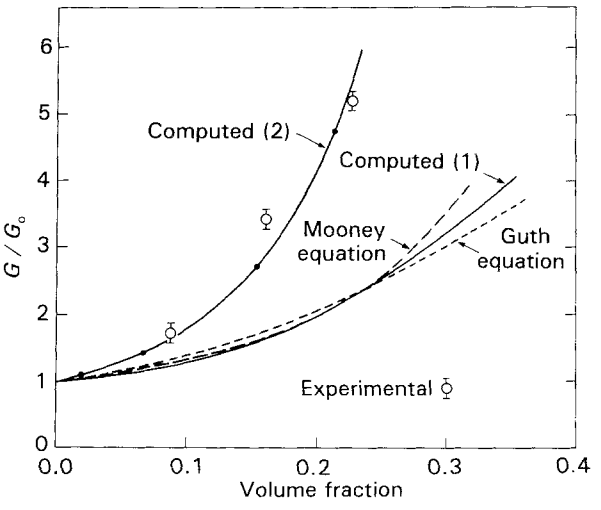

Figure 27 Plots of reduced modulus, G/G_0 against the volume fraction of filler, v: numerical and theoretical results compared with experimental ones.

5. Conclusion

Stress and strain distribution around rigid spherical fillers in elastomers subjected to uniaxial stress, computed based on the strain-energy function obtained experimentally, agree well with the classical theoretical solutions at small average strain. At large extension, however, the maximum stress concentration factor increases rapidly and the maximum strain concentration factor decreases slightly as average strain increases. These tendencies will be increased more in carbon black-filled elastomers compared with unfilled elastomers. The phenomena can be understood reasonably by considering both geometric and material non-linearity which play important roles in the deviation of α_{max} and β_{max} from the classical theoretical solutions as extension increases.

Reinforcement of elastomers with rigid spherical particles was also analysed through a numerical computation. The computed results agree with the Guth and Mooney equations at low volume fraction of fillers. In carbon black-filled elastomers, on the other hand, where the modulus is much higher than that given by the above equations, the computations give a good agreement with the experiments, considering the 20% increase in effective diameter of the filler.

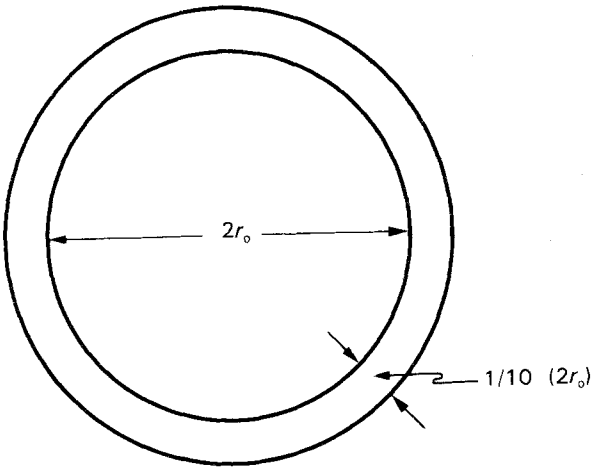

Figure 28 Schematic representation of a carbon black surrounded by the surface layer of the glassy state of rubber.

References

1. A. E. OBERTH and R. S. BRUENNER, *Trans. Soc. Rheol.* **9**(2) (1965) 165.
2. Y. FUKAHORI and W. SEKI, *J. Mater. Sci.* **28** (1993) 4143.
3. J. N. GOODIER, *Trans. ASME* **55** (1933) 33.
4. A. E. OBERTH, *Rubb. Chem. Tech.* **40** (1967) 1337.
5. A. N. GENT and B. PARK, *J. Mater. Sci.* **19** (1984) 1947.
6. K. CHO and A. N. GENT, *ibid.* **23** (1988) 141.
7. R. STRINGFELLOW and R. ABEYARATNE, *Mater. Sci. Eng.* **A112** (1989) 127.
8. A. EINSTEIN, "Investigation on Theory of Brownian Motion" (Dover, New York, 1956).
9. E. GUTH, *J. Appl. Phys.* **16** (1951) 21.
10. M. MOONEY, *J. Colloid Sci.* **6** (1951) 162.
11. Y. SATO and J. FURUKAWA, *Rubb. Chem. Tech.* **36** (1963) 1081.
12. J. J. BRENNAN and T. E. JERMYN, *J. Appl. Polym. Sci.* **9** (1965) 2749.
13. P. B. STICKNEY and R. D. FALB, *Rubb. Chem. Tech.* **37** (1964) 1299.
14. A. I. MEDALIA, *J. Colloid Interface Sci.* **32** (1970) 115.
15. G. KRAUS, *J. Polym. Sci.* **B8** (1970) 601.
16. K. FUJIMOTO and T. NISHI, *Nippon Gomu Kyokai Shi (Jpn)* **43** (1970) 465.

17. A. R. PAYNE and R. E. WHITTAKER, *Rubb. Chem. Tech.* **44** (1971) 440.
18. S. KAWABATA, M. MATSUDA, K. TEI and H. KAWAI, *Macromolecules* **14** (1981) 154.
19. W. SEKI, Y. FUKAHORI, Y. ISEDA and T. MATSUNAGA, *Rubb. Chem. Tech.* **60** (1987) 856.
20. Y. FUKAHORI and W. SEKI, *Polymer* **33** (1992) 502.
21. *Idem, ibid.* **33** (1992) 1058.
22. W. H. YANG, *J. Appl. Mech.* (1967) 942.

Received 18 May 1992
and accepted 4 January 1993